

This is the accepted manuscript made available via CHORUS. The article has been published as:

Distinct pressure evolution of coupled nematic and magnetic orders in FeSe

Anna E. Böhrer, Karunakar Kothapalli, Wageesha T. Jayasekara, John M. Wilde, Bing Li, Aashish Sapkota, Benjamin G. Ueland, Pinaki Das, Yumin Xiao, Wenli Bi, Jiyong Zhao, E. Ercan Alp, Sergey L. Bud'ko, Paul C. Canfield, Alan I. Goldman, and Andreas Kreyssig

Phys. Rev. B **100**, 064515 — Published 20 August 2019

DOI: [10.1103/PhysRevB.100.064515](https://doi.org/10.1103/PhysRevB.100.064515)

Distinct pressure evolution of coupled nematic and magnetic order in FeSe

Anna E. Böhrer,^{1,2,*} Karunakar Kothapalli,^{1,3,4,*} Wageesha T. Jayasekara,^{1,3} John M. Wilde,^{1,3} Bing Li,^{1,3} Aashish Sapkota,^{1,3} Benjamin G Ueland,^{1,3} Pinaki Das,^{1,3} Yumin Xiao,⁵ Wenli Bi,^{6,7} Jiyong Zhao,⁶ E. Ercan Alp,⁶ Sergey L. Bud'ko,^{1,3} Paul C. Canfield,^{1,3} Alan I. Goldman,^{1,3} and Andreas Kreyssig^{1,3}

¹*Ames Laboratory, U.S. DOE, Iowa State University, Ames, Iowa 50011, USA*

²*Institut für Festkörperphysik, Karlsruhe Institute of Technology, 76021 Karlsruhe, Germany*

³*Department of Physics and Astronomy, Iowa State University, Ames, Iowa 50011, USA*

⁴*College of Arts and Sciences, King University, Bristol, Tennessee, 37620, USA*

⁵*HPCAT, X-ray Science Division, Argonne National Laboratory, Argonne, IL 60439, USA*

⁶*Advanced Photon Source, Argonne National Laboratory, Argonne, Illinois 60439, USA*

⁷*Department of Geology, University of Illinois at Urbana-Champaign, Urbana, Illinois 61801, USA*

We present a microscopic study of nematicity and magnetism in FeSe over a wide temperature and pressure range using high-energy x-ray diffraction and time-domain Mössbauer spectroscopy. The low-temperature magnetic hyperfine field increases monotonically up to ~ 6 GPa. The orthorhombic distortion initially decreases under increasing pressure, but is stabilized at intermediate pressures by cooperative coupling to the pressure-induced magnetic order. Close to the reported maximum of the superconducting critical temperature at $p = 6.8$ GPa, the orthorhombic distortion suddenly disappears and a new tetragonal magnetic phase occurs. The pressure and temperature evolution of the structural and magnetic order parameters suggests that they have independent origins.

I. INTRODUCTION

A fascinating characteristic of iron-based superconductors is their complex phase diagrams, and a decade of research has revealed intricate relationships between magnetism, structure and superconductivity. The typical stripe-type antiferromagnetic order¹ breaks the tetragonal lattice symmetry and, hence, causes an orthorhombic lattice distortion². But there are two intriguing exceptions to this close coupling between structure and magnetism. First, the orthorhombic distortion can decouple from the stripe-type magnetic order and occurs at a higher temperature ($T_s > T_N$) in many materials^{3–6}. This observation is at the origin of the idea of magnetic-fluctuation-induced nematicity^{7–9}. Second, magnetic order can also occur without any orthorhombic lattice distortion, as observed in certain hole-doped iron-based systems^{10–19}. This "C4-type" tetragonal magnetic phase was shown to arise from a coherent superposition of the two symmetry-equivalent, stripe-type antiferromagnetic propagation vectors¹⁷.

FeSe has generated enormous interest over the past few years as an extreme case of nematicity^{20–29} with its tetragonal-to-orthorhombic transition close to $T_s = 90$ K and no magnetic order down to sub-Kelvin temperatures³⁰. FeSe has also generated excitement due to the high tunability of its superconducting transition temperature T_c , which reaches from a modest $T_c \sim 8$ K³¹ at ambient pressure to $T_c = 37$ K at $p \sim 6.3$ GPa³². The temperature-pressure phase diagram of FeSe is, in fact, rather complex [Fig. 1(a)]. T_s is initially suppressed under pressure^{33–36} and pressure-induced magnetic order emerges for $p > 0.8$ GPa^{30,32,34,35,37}. The structural and magnetic phase lines merge into a concomitant magneto-structural transition at 1.7 GPa³⁵. This suggests that the magnetic ground state is orthorhom-

bic and presumably of the same stripe type as occurs in other iron-based materials, as also suggested by NMR and μ SR results^{36,38}. The magneto-structural transition traces out a dome with increasing pressure, with a maximum of $T_N = 45$ K around 5 GPa³². The origins of the large extent of nematicity and of the high T_c in the pressure-temperature phase diagram of FeSe remain enigmatic and ask for a microscopic study that covers the full pressure range.

Here, we present a microscopic investigation of the magnetic order, crystallographic symmetry, and in-plane lattice parameters of FeSe under hydrostatic pressure up to 10 GPa. We find evidence for a tetragonal magnetic ground state around 6 – 7 GPa (where T_c is maximized), which means that FeSe can be tuned through multiple types of magneto-structural coupling. The pressure- and temperature dependent orthorhombic distortion and magnetic hyperfine field suggest that the two ordering phenomena have distinct origins in FeSe, although they couple cooperatively.

II. METHODS

Single-crystals of FeSe were prepared by chemical vapor transport as described in Ref. 39. Batch A samples are from several similar batches using natural-abundance elements, whereas batch B samples are from a batch prepared using 95% enriched ⁵⁷Fe. High-energy (100 keV), high-resolution x-ray diffraction experiments over a pressure range of $p = 0$ –10 GPa were performed at station 6ID-D of the APS, Argonne, on samples from batches A and B using diamond anvil cells with He gas as a hydrostatic pressure-transmitting medium. The spot illuminated by our x-ray beam was optimized for equal domain population at low temperature. Data taken on different spots of the sample yield consistent results. The

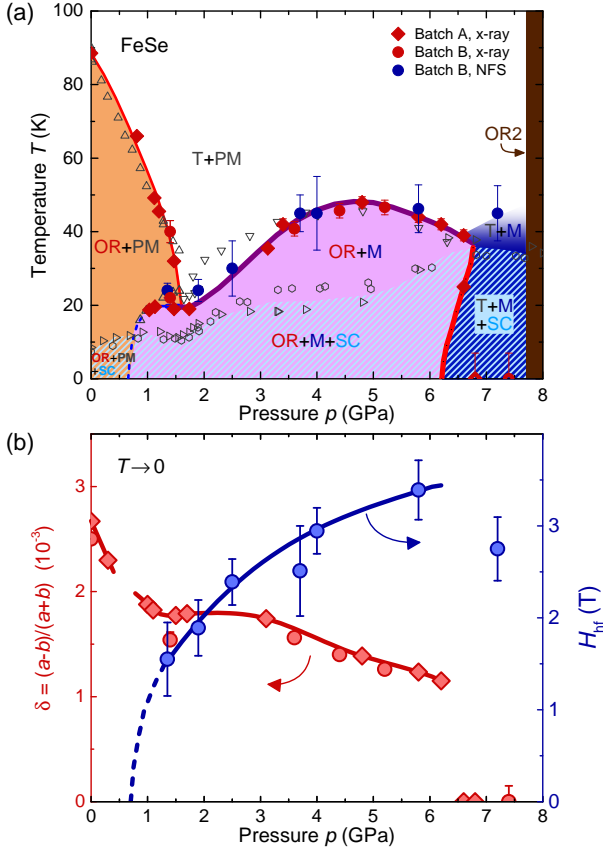


FIG. 1. (a) Temperature-pressure phase diagram of FeSe. The structural transition temperatures were obtained by x-ray diffraction measurements on two different batches: A (red circles) and B (red diamonds). T (OR) stands for the tetragonal (orthorhombic) phase, OR2 for the high-pressure orthorhombic phase (see⁴⁰ for details on the OR2 phase) and SC for the superconducting state. PM (M) indicates paramagnetic (magnetically ordered) regions of the phase diagram as determined from nuclear-forward-scattering experiments on samples from batch B, with the transition temperature indicated by blue circles. Thick (thin) lines represent first (second) order phase transitions, respectively. Data from other reports (gray open symbols) are shown for comparison and completeness: up triangles⁴¹ and down triangles³² indicate the structural and magneto-structural transitions, right triangles³² and hexagons³³ indicate the superconducting transition. (b) Pressure-dependence of the zero-temperature limit of the orthorhombic distortion, i.e., the structural order parameter (left axis), and the hyperfine field (right axis), as a proxy for the magnetic order parameter. Solids lines are a guide to the eye, the dashed line indicates an extrapolation based on Ref.³⁰

lattice parameter of polycrystalline silver was used for in-situ pressure determination at all temperatures, so that the actual temperature dependent pressure values are reported. Nuclear forward scattering (NFS), i.e., time-domain Mössbauer spectroscopy, was performed on samples from batch B in diamond anvil cells with He gas

as pressure medium and ruby as in-situ pressure calibrant. All pressure values have an accuracy of ~ 0.2 GPa, though pressure changes of less than 0.05 GPa can be resolved during a temperature sweep. Spectra for $2.5 \text{ GPa} \leq p \leq 7.2 \text{ GPa}$ were collected at station 16ID-D at the APS in its standard timing mode with a pulse periodicity of 153 ns. Spectra for $p < 2.5 \text{ GPa}$ were collected at station 3ID-B in the so-called hybrid mode with a $1.5 \mu\text{s}$ clear time after the initial excitation pulse, improving the sensitivity and precision of determining the internal magnetic hyperfine field, but reducing the counting rate. Spectra were analyzed with the program CONUSS⁴². (See⁴⁰ for further experimental details.)

III. RESULTS

Figure 1 summarizes the experimental results. In the temperature-pressure phase diagram (a), the nematic, i.e., orthorhombic-paramagnetic (OR+PM), region on the low-pressure side borders an orthorhombic magnetically-ordered (OR+M) dome. We find that magnetic order persists on the high-pressure side of the magnetic dome in the absence of an orthorhombic distortion (T+M). The phase diagram is "cut off" at $p = 7.7 \text{ GPa}$ when the layered structure of FeSe becomes unstable and the material undergoes a first-order structural transition into another orthorhombic "OR2" phase^{40,43,44}. The low-temperature values of the magnetic and structural order parameters are shown in Fig. 1(b). The ordered magnetic hyperfine field increases monotonically over the orthorhombic-magnetic dome, whereas the orthorhombic distortion of the FeSe layers has a complex pressure dependence. It decreases initially on increasing pressure and barely changes between 1 – 3.4 GPa, before gradually decreasing again and vanishing abruptly for $p > 6.6 \text{ GPa}$.

Figure 2(a) shows the high-energy x-ray diffraction data of samples from batch A close to $(H H 0)$ -type Bragg peaks, which reveal the temperature and pressure dependence of the orthorhombic distortion. A detailed comparison of the diffraction data of the two batches is reported in the supplemental material⁴⁰. The ambient-pressure second-order transition at T_s is suppressed under pressure. At $p = 1.5 \text{ GPa}$, a first-order transition is apparent at $T_N < T_s$ and the two transitions merge for slightly higher pressures, as already reported in Ref. 35. Notably, the merged first-order transition is observed in the same manner up to 5.8 GPa, but a new behavior emerges at higher pressures, most prominently at $p = 6.6 \text{ GPa}$. On decreasing temperature, the sample first undergoes the first-order tetragonal-to-orthorhombic transition, at $T_{s,N} = 39 \text{ K}$, before it transforms back into a tetragonal structure at $T_r = 25 \text{ K}$, exhibiting "structural reentrance". At the just slightly higher pressure of 6.8 GPa, the sample remains tetragonal at all temperatures. We note that a small phase fraction ($\lesssim 15\%$) appears to become orthorhombic in a limited temper-

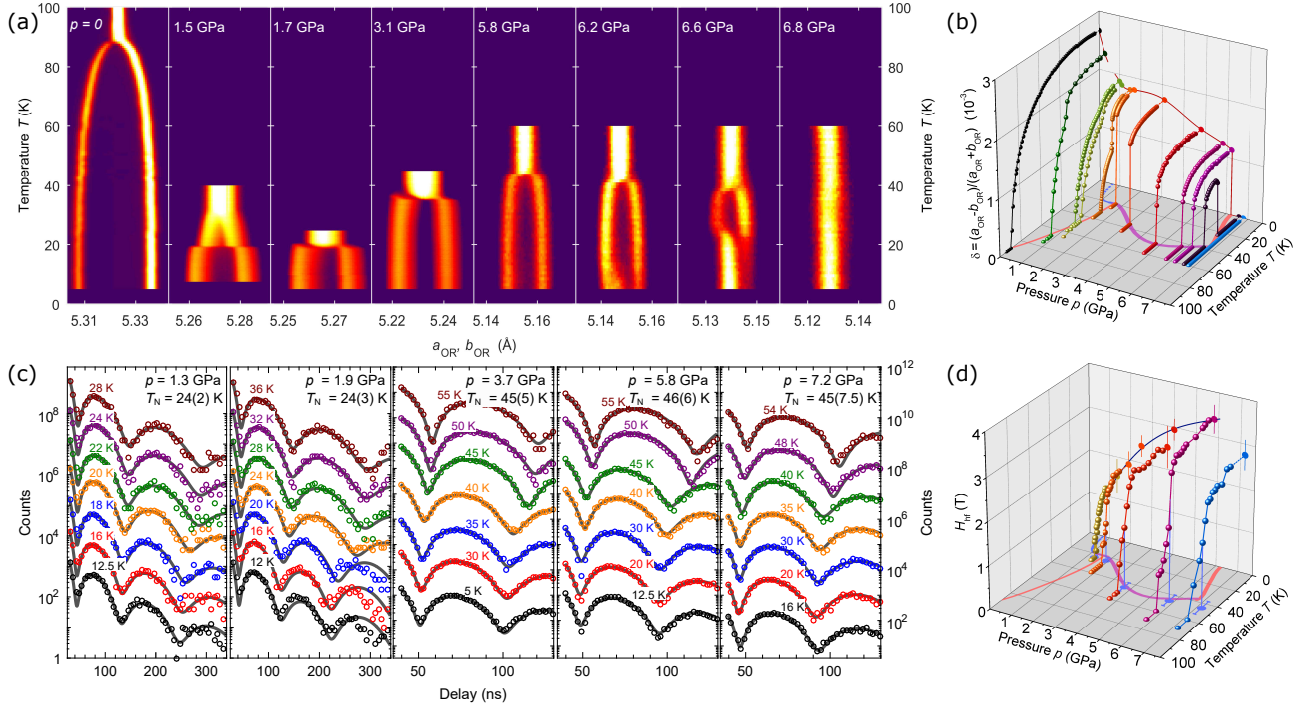


FIG. 2. (a) The detector intensity for positions spanning the (3 3 0) or (6 6 0) tetragonal unit cell Bragg peaks integrated over the transverse scattering directions at various pressures, revealing the temperature dependence of the in-plane orthorhombic lattice parameters a_{OR} and b_{OR} . Low-pressure ($p \leq 3.1$ GPa) data are taken from Ref. 35. (b) Three-dimensional representation of the temperature- and pressure-dependence of the orthorhombic distortion, $\delta = (a_{\text{OR}} - b_{\text{OR}})/(a_{\text{OR}} + b_{\text{OR}})$. Projections of the extrapolated low-temperature values [1(b)] are shown in the $T = 0$ plane. Lines are guides to the eye. The phase diagram from Fig. 1(a) is indicated in the basal, $T - p$ plane. (c) ^{57}Fe nuclear-forward-scattering spectra for FeSe at selected pressures and temperatures. Data are offset for clarity, and dark gray lines show fits to the data using CONUSS⁴². (d) Three-dimensional representation of the temperature- and pressure-dependence of the inferred magnetic hyperfine field, H_{hf} , analogous to (b).

ature range even at 6.8 GPa, apparently experiencing a slightly lower effective pressure due to small internal stresses. Similarly, at the lower pressure of 6.2 GPa, a tetragonal fraction of the sample ($\sim 20\%$) coexists with the major orthorhombic phase at base temperature and transforms to orthorhombic at ~ 12 K on heating [see Fig. 2(a)]. Figure 2(b) summarizes the complex temperature and pressure evolution of the orthorhombic order parameter $\delta = (a_{\text{OR}} - b_{\text{OR}})/(a_{\text{OR}} + b_{\text{OR}})$. Notably, δ behaves as the order parameter of a first-order structural transition over a large pressure range 2 – 5.8 GPa. The structurally “reentrant” behavior with vanishing lattice distortion at the lowest temperatures is limited over the pressure range $6.2 \lesssim p < 6.8$ GPa and the orthorhombic distortion is absent at all temperatures at 6.8 GPa.

Figure 2(c) shows the NFS spectra at various pressures up to 7.2 GPa, from which the information about the magnetic order is obtained. The observed quantum beats originate from a convolution of the hyperfine field, quadrupole splitting and sample thickness. Data for $p < 2$ GPa were collected on a 6 μm thick sample and higher-pressure data were collected on an 18 μm thick sample. A temperature-induced change in the spectra, most notably the shift of the minima, e.g., between 20

K and 24 K at 1.9 GPa, indicates the magnetic phase transition. Such a transition is observed for pressures up to 7.2 GPa. At 1.3 GPa a similar, though more continuous shift is discernible and identified as a second-order magnetic phase transition.

The inferred magnetic hyperfine field reported in Fig. 2(d) appears to indicate first-order transitions broadened by internal stresses or disorder for $p > 2$ GPa. Interestingly, magnetic order is observed up to 7.2 GPa, where the orthorhombic distortion vanishes. This indicates the presence of a tetragonal magnetically ordered phase. The occurrence of such a phase, including a “structurally reentrant” behavior is highly reminiscent of the hole-doped 122-type materials with a “C4” magnetic phase^{15,17,19,45}. We note that the tetragonal magnetic state in $(\text{Sr},\text{Na})\text{Fe}_2\text{As}_2$ was shown to be a coherent superposition of two spin-density waves and is characterized by two distinct Fe sites – one with zero and one with double the hyperfine field of the regular stripe-type phase¹⁷. Unfortunately, in contrast to conventional Mössbauer spectroscopy, our time-domain Mössbauer spectroscopic experiment is unable to distinguish such a state from a state with the same hyperfine field on all Fe sites. Here, we show the results of fitting with a single H_{hf} . An equally

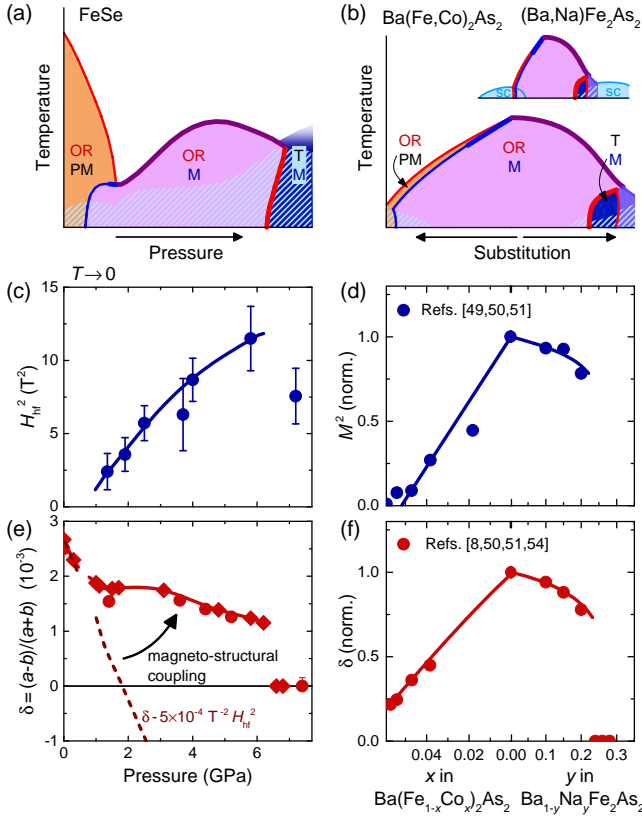


FIG. 3. (a), (b) Schematic phase diagrams of FeSe under pressure (this work) and BaFe_2As_2 doped with cobalt (Ref. 4, 8, and 47) and sodium (Ref. 48), a larger doping range is shown in the inset. Phase lines and phases are color-coded and labelled as in Fig. 1(a). (c)-(f) Evolution of the orthorhombic and magnetic order parameters of FeSe and BaFe_2As_2 . (c) Square of hyperfine field H_{hf}^2 of FeSe under pressure. (d) Square of the ordered magnetic moment of $\text{Ba}(\text{Fe},\text{Co})_2\text{As}_2$ ⁴⁹ and $(\text{Ba},\text{Na})\text{Fe}_2\text{As}_2$ ^{50,51}. (e) Low-temperature extrapolation of δ of FeSe as a function of pressure. The dashed line shows the experimental δ subtracted by a contribution proportional to H_{hf}^2 , which smoothly continues the initial trend of $\delta(p)$. The enhancement of δ from this line is attributed to the cooperative magneto-structural coupling δM^2 , expected in a Landau theory^{2,7,52,53}. (f) Low-temperature extrapolation of δ of $\text{Ba}(\text{Fe},\text{Co})_2\text{As}_2$ (Refs. 8 and 54) and $(\text{Ba},\text{Na})\text{Fe}_2\text{As}_2$ (Refs. 50 and 51). Lines are a guide to the eye. The data from different references in (d), (f) are scaled at pure BaFe_2As_2 .

good fit of our data at 7.2 GPa can be achieved with a model in which zero moment is imposed for half of the Fe sites and $H_{\text{hf}} \approx 4.5$ T on the moment-bearing Fe-sites at base temperature. It is also possible that a completely different type of magnetic order is realized, as might be indicated by the presence of Néel type magnetic fluctuations at ambient pressure⁴⁶.

IV. DISCUSSION

The schematic temperature-pressure phase diagram of FeSe has remarkable topological similarities to the temperature-substitution phase diagram of the canonical BaFe_2As_2 iron-based superconductors [see Figs. 3 (a), (b)]. FeSe at low pressures and slightly underdoped $\text{Ba}(\text{Fe},\text{Co})_2\text{As}_2$ both have an orthorhombic paramagnetic ground state. On increasing pressure or decreasing Co content the ground state changes to orthorhombic and antiferromagnetic within a region for which $T_s > T_N$ until the structural and magnetic phase lines merge. On the high-pressure side of FeSe and in close to optimally doped $(\text{Ba},\text{Na})\text{Fe}_2\text{As}_2$ a tetragonal magnetic ground state emerges. The qualitative difference between FeSe under pressure and substituted BaFe_2As_2 is evident in the relative slopes of the phase lines and, notably, in the values of the orthorhombic and magnetic order parameters [see Figs. 3 (c)-(f)]. Whereas the order parameters in the 122-type systems (approximately) obey linear-quadratic coupling, $\delta \propto M^2$, which is theoretically expected based on symmetry considerations in a Landau theory^{2,7,52,53}, this is not the case for FeSe.

One way to rationalize our results on FeSe is to assume that the material's structural instability and its magnetic order have distinct origins and that the structural instability is weakened whereas the magnetic instability is strengthened with increasing pressure. The low cost of orthorhombic distortion at lower pressures likely favors a stripe-type antiferromagnetic order. The symmetry-imposed cooperative magnetoelastic coupling of orthorhombic distortion and stripe-type magnetic order then causes an increase of δ from its initial trend that is $\propto M^2$, as indicated by the arrow in Fig. 3(e). Above ~ 6.6 GPa the orthorhombic distortion becomes so unfavorable that the cooperative coupling to stripe-type magnetic order can no longer create a finite distortion and, instead, tetragonal magnetic order is established. Interestingly, in lightly S-doped FeSe, the orthorhombic distortion and the pressure-induced magnetic order indeed occur in distinct regions of the pressure-temperature phase diagram⁵⁵⁻⁵⁷.

Theoretically, the nematic order of FeSe at ambient pressure has been suggested to arise from a Pomeranchuk instability within a renormalization group analysis⁵⁸, which could explain the observed result. The theoretically proposed antiferroquadrupolar order⁵⁹ is another candidate. The effect of pressure as a tuning parameter for FeSe has been subject to numerous theoretical studies as well^{24,60-62}. Model⁶¹ and ab-initio⁶² calculations find a decrease of the tendency to charge order under pressure that could be associated with our results.

In Figs. 1 and 3(a), we also report the superconducting transition temperature T_c from Refs.³² and³³, revealing T_c is maximized in the pressure range of the tetragonal magnetic phase. Possibly, T_c is enhanced by the enlarged magnetic fluctuations space due to the presence of several almost degenerate magnetic orders, as conjectured for

optimally hole-doped iron-pnictides⁶³.

V. CONCLUSION

In summary, we have studied the structural and magnetic phase diagram and order parameters of FeSe. We have exposed the complex behavior of the orthorhombic distortion, including structural reentrance at 6.6 GPa, and the unexpected occurrence of magnetic order within an undistorted tetragonal lattice. The pressure evolution of the magnetic and structural transition temperatures and order parameters of FeSe leads us to suggest that the orthorhombic distortion and the magnetic order have distinct origins. Nevertheless, the topology of the temperature-pressure phase diagram of FeSe resembles closely the well-known phase diagram of electron/hole-doped BaFe_2As_2 , due to the symmetry-imposed coupling of the two order parameters. The high-temperature superconductivity in FeSe under pressure emerges within this rich magneto-structural phase diagram in the region of two almost degenerate magnetic orders.

VI. ACKNOWLEDGEMENTS

We would like to acknowledge the assistance of D. S. Robinson, C. Benson, S. Tkachev, S. G. Sinogeikin, Ross Hrubciak, Barbara Lavina, R. Somayazulu and M. Baldini, and helpful discussions with Dominic Ryan and R. J. McQueeney. Work at the Ames Laboratory was supported by the Department of Energy, Basic Energy Sciences, Division of Materials Sciences & Engineering, under Contract No. DE-AC02-07CH11358. This research used resources of the Advanced Photon Source, a U.S. Department of Energy (DOE) Office of Science User Facility operated for the DOE Office of Science by Argonne National Laboratory under Contract No. DE-AC02-06CH11357. HPCAT operations are supported by DOE-NNSA's Office of Experimental Sciences. Use of the COMPRES-GSECARS gas loading system was supported by COMPRES under NSF Cooperative Agreement EAR 11-57758 and by GSECARS through NSF grant EAR-1128799 and DOE grant DE-FG02-94ER14466. W.B. acknowledges the partial support by COMPRES, the Consortium for Materials Properties Research in Earth Sciences under NSF Cooperative Agreement EAR 1606856.

Appendix A: Detailed experimental methods

Single crystals of FeSe were prepared by chemical vapor transport as described in Ref. 39. Batch A samples are from several batches using natural-abundance elements, whereas batch B samples are from a batch prepared using 95% enriched ^{57}Fe . As described in Ref. 39, the sample properties can vary even with tiny variations in growth

conditions. Batch B was found to have less perfect mosaicity and less sharp phase transitions than samples from batch A, however batch A and B both have very similar transition temperatures and values for the orthorhombic distortion (see Fig. 1 of the main paper).

High-energy (100 keV), high-resolution x-ray diffraction experiments were performed at station 6ID-D of the APS Argonne on samples from batches A and B. The samples were pressurized in diamond anvil cells (DACs) using He gas as a hydrostatic pressure-transmitting medium. We used diamonds with 600 μm culets and stainless-steel and CuBe gaskets preindented to thicknesses of ~ 60 μm and with laser-drilled holes of ~ 250 – 350 μm . The position of a fluorescence line for ruby was used for ambient-temperature pressure calibration. Measurements of the lattice parameter of polycrystalline silver were used for in-situ pressure determination at all temperatures, so that the actual temperature-dependent pressure values are reported. The absolute error on the pressure values is estimated to be ± 0.2 GPa, but much smaller pressure changes of less than 0.05 GPa can be resolved during a temperature or pressure sweep.

Extended regions of selected reciprocal lattice planes of FeSe and the powder diffraction pattern of silver were recorded by a MAR345 image plate system positioned 1.474 m behind the DAC, as the DAC was rocked by up to $\pm 3.2^\circ$ about two independent axes perpendicular to the incident x-ray beam. High-resolution diffraction patterns of selected FeSe Bragg reflections of samples from batch A were also recorded using a Pixirad-1 detector positioned 1.397 m behind the DAC while rocking the sample around one of the two axes perpendicular to the x-ray beam. The in-plane lattice parameters were determined by fitting the Bragg peak positions after integrating the data over the transverse scattering directions. This procedure was used for both the data recorded by the Pixirad-1 detector and by the MAR345 image plate system.

For the nuclear forward scattering experiments, the nuclear decay signal of ^{57}Fe nuclei excited by a synchrotron pulse carries the signature of hyperfine interactions such as internal hyperfine magnetic field, electric quadrupole interaction, and crystal orientation. (The latter becomes relevant because the incident synchrotron beam is polarized in the horizontal plane, and it is narrowly collimated.) The time beats observed in the spectra are the time-domain Fourier transform of multiple nuclear resonances between sub-states of the ground state (spin 1/2) and the first excited state (spin 1/2). By fitting the data to the full Hamiltonian, the transition energies and their amplitudes are calculated. The theoretical description is given in more detail in Ref.⁴².

The nuclear forward scattering (NFS), i.e. time-domain Mössbauer spectroscopy, was performed on stations 3ID-B and 16ID-D at the Advanced Photon Source (APS) on samples from batch B. Diamond anvil cells with He as a pressure transmitting medium and ruby as an in-situ pressure calibrant were used and the pressure

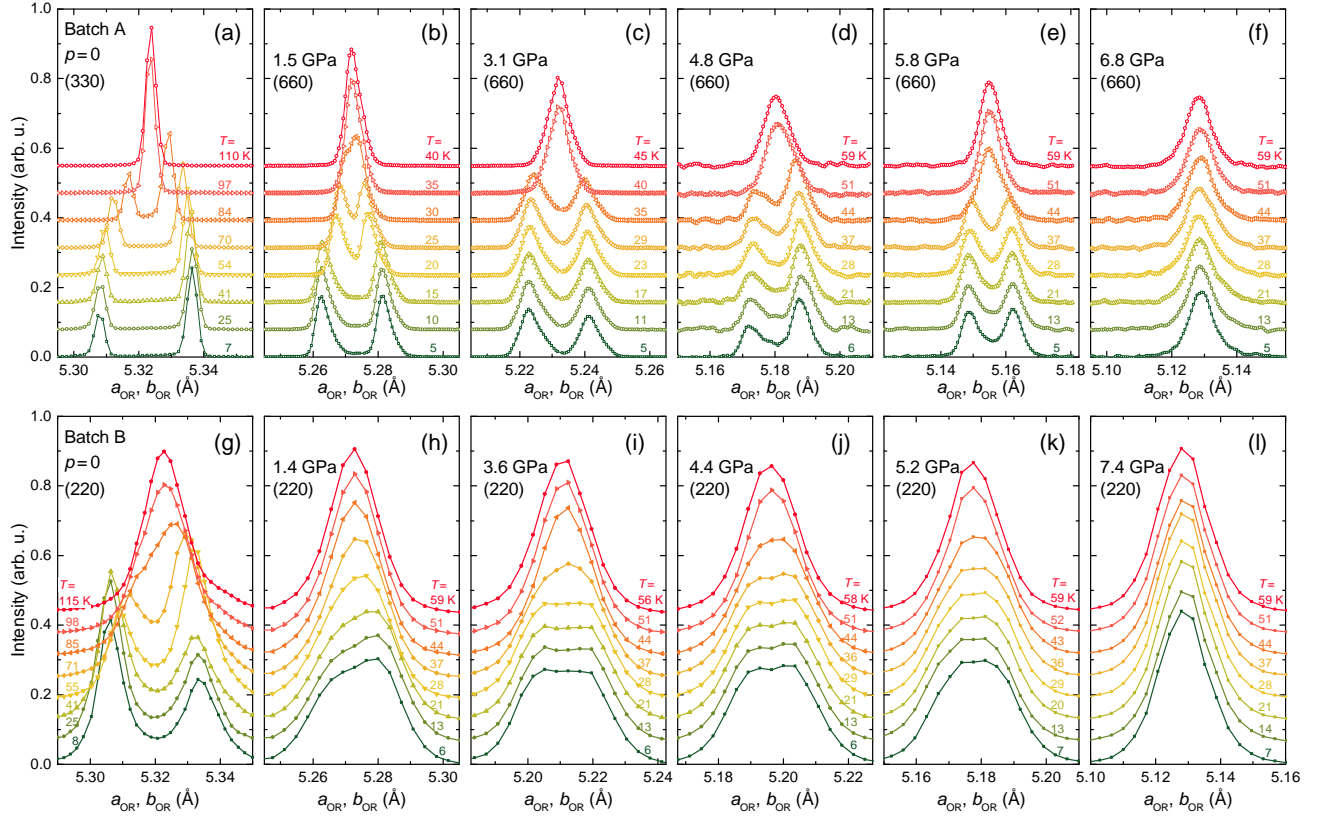


FIG. 4. High-energy x-ray diffraction patterns demonstrating the tetragonal to orthorhombic phase transition. a_{OR} and b_{OR} are the lattice parameters for the orthorhombic unit cell (a)-(f), X-ray intensity profiles taken across the (3 3 0) (a) and (6 6 0) [(b)-(f)] tetragonal unit cell Bragg peaks on samples from batch A for various pressures and temperatures. The peak splitting results from the orthorhombic distortion. (g)-(l), X-ray intensity profiles close to the (2 2 0) Bragg peaks for samples from batch B at various pressures and temperatures. Here, the peak splitting or broadening signals the orthorhombic distortion. The difference in peak profiles with respect to the upper panels results from the lower order of the chosen Bragg peak, the use of a different detector, and the broader mosaicity of samples from batch B.

cells were set up in a similar way as for the diffraction experiments. At 3ID-B, miniature panoramic DACs⁶⁴ were used. The incident x-ray beam was monochromated to the ^{57}Fe nuclear resonance energy of 14.4125 keV with a resolution of 2 meV and the intensity of the scattered beam in the forward direction was recorded by an Avalanche Photo Diode detector. The beam size at 3ID-B and 16ID-D was $10 \times 10 \mu\text{m}^2$ and $20 \times 30 \mu\text{m}^2$, respectively.

Spectra for $p \geq 2.5$ GPa were collected at 16ID-D on an $18 \mu\text{m}$ thick sample using the 24-bunch standard timing mode of the APS, where an x-ray pulse of 80 ps duration hits the sample with a periodicity of 153 ns. Spectra for $p < 2.5$ GPa were collected at 3ID-B beamline on a $6 \mu\text{m}$ thick sample in the so-called hybrid mode with a $1.5 \mu\text{s}$ clear time for measurements after the initial excitation pulse hits the nuclei. This long-pulse mode reduces the counting rate by an order of magnitude. However, it drastically improves the sensitivity and precision of determining the internal magnetic hyperfine field due to the increased observation time of the nuclear decay, which is particularly relevant when hyperfine fields are very small.

The program CONUSS⁴² was used to analyze the spectra and determine the magnetic field hyperfine at the iron sites. Note that the fitted hyperfine field and quadrupole splitting values are somewhat correlated and neither energy domain, nor time domain, spectroscopy can easily separate them. At each pressure, we have determined a value of the quadrupole splitting at $T > T_N$ and kept it constant for all temperatures. The values of the quadrupole splitting are 0.1 – 0.2 mm/s.

Appendix B: Detailed x-ray diffraction data and comparison of the two batches

In Fig. 4 data on samples from batches A (obtained with the Pixirad-1 detector) and B (obtained with the MAR345 detector) are compared. An obvious difference in peak profiles results from the different orders of the chosen Bragg peaks, the use of different detectors, and the broader mosaicity of samples from batch B. A low-temperature peak-splitting or broadening indicates an orthorhombic ground state. Structural transitions are

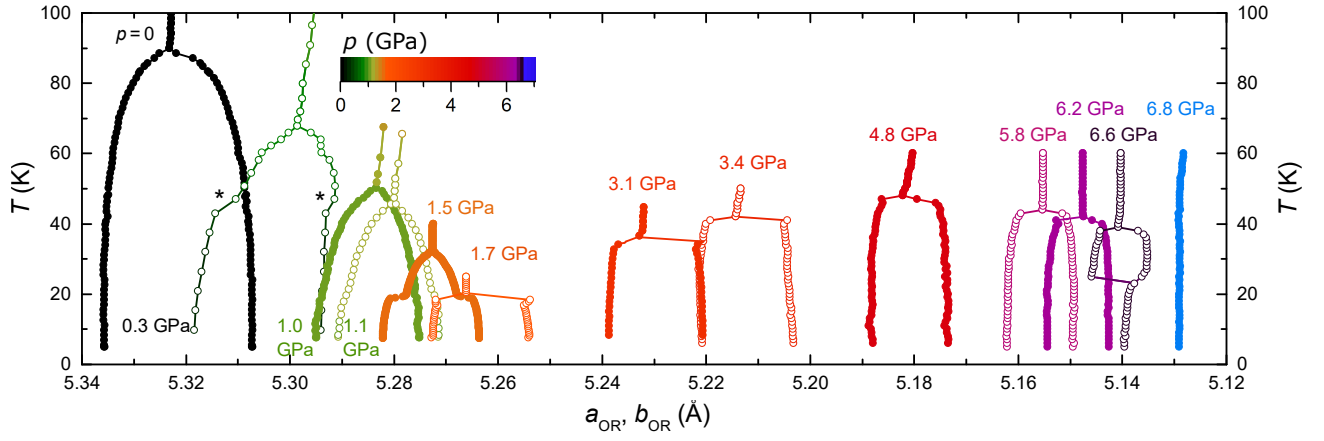


FIG. 5. Orthorhombic lattice parameters a_{OR} and b_{OR} as a function of temperature for various pressures. Stars mark the crossing of the He-solidification line, which entails a change in pressure (see color scale). Note that the horizontal scale decreases from left to right.

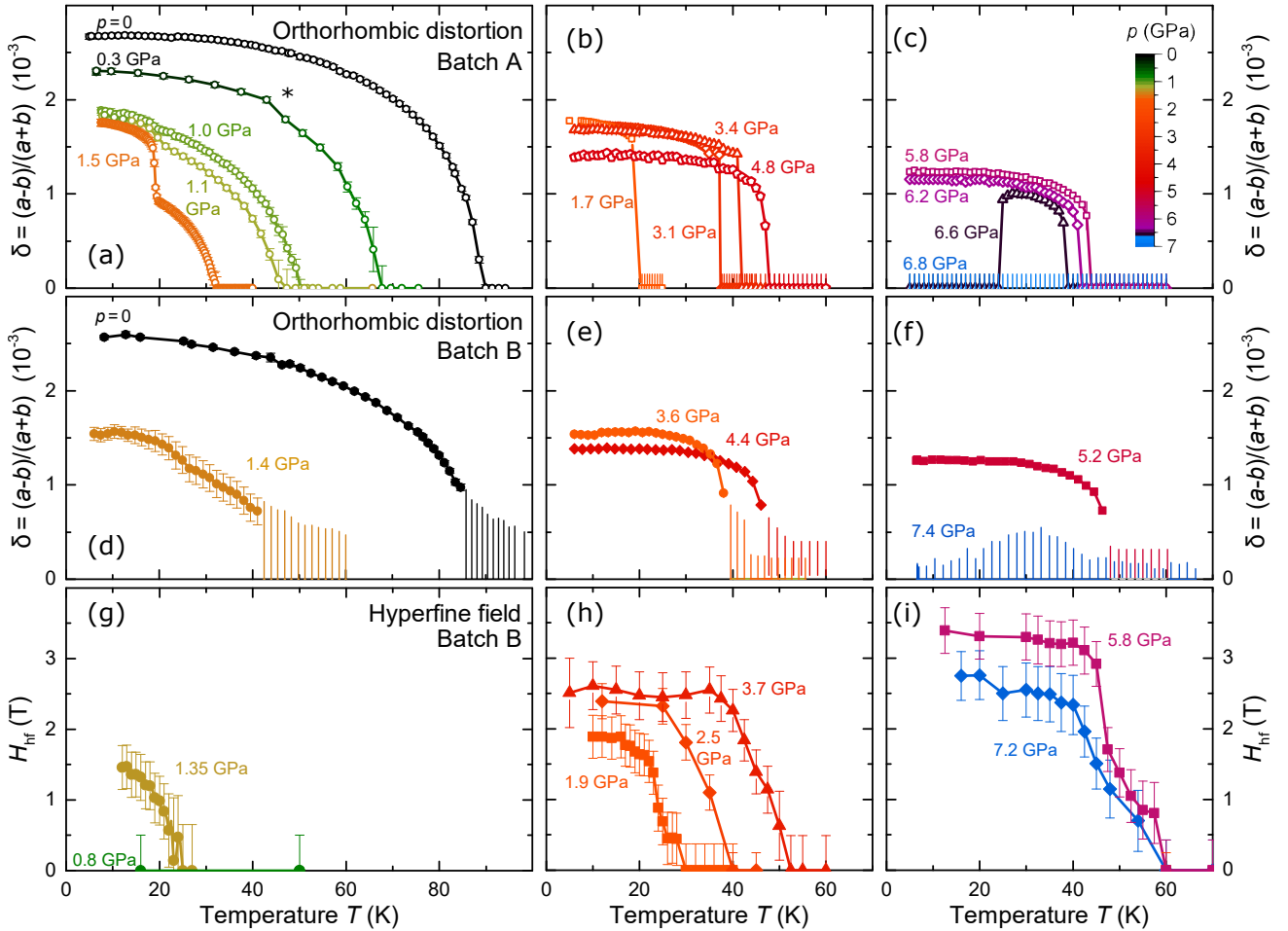


FIG. 6. (a)-(c) Orthorhombic distortion δ of samples from batch A as a function of temperature at various color coded pressures [see scale in (c)]. The star symbol in (a) marks the crossing of the He solidification line, labelled pressures are at base temperature. (d)-(f) Orthorhombic distortions δ of samples from batch B. Vertical bars represent a possible inhomogeneous distortion above the midpoint of the structural transition deduced from peak broadening. (g)-(i) Hyperfine field H_{hf} at the Fe site for samples from batch B, determined from the fitting shown in Fig. 2(c) of the main paper. Data at 2.5 GPa from Ref. 35 are also reported. Error bars represent the estimated total uncertainty including systematic errors.

clearly visible for samples from both batches. At the highest pressures of 6.8 and 7.4 GPa, the absence of any peak splitting or broadening and the temperature independent peak profiles up to 60 K indicate a tetragonal ground state.

Figure 5 shows the in-plane lattice parameters of the majority phase of FeSe vs. temperature for all the studied pressures. FeSe has a high compressibility and the tetragonal in-plane lattice parameter is decreased by 3.7% at 7 GPa. In the pressure range 1.7-4.8 GPa, the orthorhombic transition results in an asymmetric change of in-plane lattice parameters so that the average of the a and b lattice constants decreases at the transition, similar to the $\text{Ba(Fe,Co)}_2\text{As}_2$ system⁶⁵. This reverses at higher pressures, so that at ~ 6 GPa, the a - b average increases on cooling through T_s , similarly to underdoped $(\text{Ba,K})\text{Fe}_2\text{As}_2$ ¹².

In Fig. 6, we also compare the diffraction results for the two different batches and show the inferred hyperfine fields for batch B. The transitions are very sharp in samples from batch A, whereas samples from batch B exhibit clear tails to the transitions, which likely arise from inhomogeneities caused by internal stresses. The hyperfine fields deduced from the NFS spectra in Fig. 3(h),(i) exhibit similar tails, likely of the same origin. Nevertheless, transition temperatures can be well defined as the points of highest rate change of order parameters and the thus determined values of T_s agree well between the two batches (see Fig. 1(a) of the main paper).

Appendix C: High-pressure phase of FeSe

At just slightly higher pressures than those presented in Fig. 6 the samples of both batches undergo a severe structural transition illustrated in Fig. 7. This transition is well-known in literature^{43,44,66–68} and the high-pressure orthorhombic "OR2" phase has been identified as having MnP-type structure with a dramatic volume reduction of $\sim 10\%$ with respect to the layered PbO-type FeSe phase that is stable at lower pressures. Its unit cell is tilted with respect to the T and OR phases. The inset in Fig. 7(a) shows sections of the $(HK0)$ scattering plane of the two phases at representative pressures. The sharp $(110)_T$ Bragg peaks of the tetragonal phase completely disappear in the high-pressure OR2 phase. The latter is characterized by 8 much broader $(101)_{\text{OR2}}$ type reflections, indicating significant sample degradation which is clearly due to the huge volume reduction and build-up of stress due to domains of the MnP-type structure with different orientations. We have observed this transition in measurements with increasing pressure at constant temperatures 60 K, 150 K and 300 K, in three different samples (from batch A) and also on temperature increase (concomitant with a slight pressure increase, see path 4 in the Fig. 7) in a sample from batch B. The fine

pressure steps along path 3 allow to resolve particularly well the rapidly changing OR2 phase fraction between

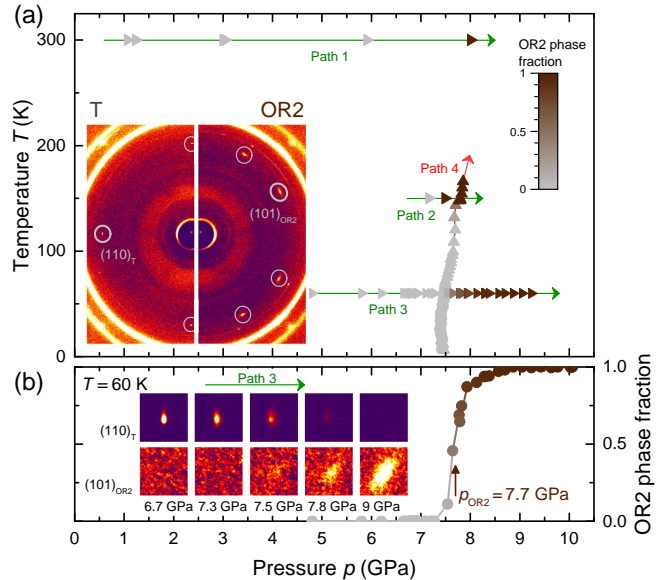


FIG. 7. High-pressure structural transition of FeSe. (a) Points in the temperature-pressure phase diagram of FeSe with the fraction of the OR2 phase color-coded. The transition into the OR2 phase was observed to be abrupt and irreversible. The inset shows sections of the $(HK0)$ diffraction plane in the T and OR2 phases. The $(110)_T$ and $(101)_{\text{OR2}}$ and symmetry-equivalent reflections are highlighted by gray circles. (b) Phase fraction of the OR2 phase as evaluated by the relative intensity of the $(101)_{\text{OR2}}$ with respect to the $(110)_T$ Bragg reflections on increasing pressure at constant $T = 60$ K (path 3). The insets show the area surrounding these Bragg reflections at representative pressures.

$p = 7.5 - 8.5$ GPa. Together, these four independent measurements define a sharp and nearly temperature-independent phase line at $p \approx 7.7$ GPa. We found this transition to have a severe hysteresis and to cause irreversible changes to the single-crystalline sample. For example, no return to the tetragonal phase was observed even after decreasing pressure down to 3 GPa and increasing temperature to 300 K following the measurement along path 2.

In previous reports using polycrystalline material^{43,66,67} and in a single-crystal study with glycerol pressure medium³², the structural transition into the OR2 phase has been observed at $p \sim 10 - 12$ GPa and often with a significant phase coexistence range. Our lower critical pressure is, however, close to the one reported in Refs. 44 and 68, which also used single crystals and He as pressure medium. This transition into a much more closely-packed crystal structure at high pressures marks the end of the stability of the layered structure of FeSe that shares its structural motif with iron-arsenide superconductors.

- * These authors contributed equally.
- ¹ P. Dai, *Rev. Mod. Phys.* **87**, 855 (2015).
 - ² A. Cano, M. Civelli, I. Eremin, and I. Paul, *Phys. Rev. B* **82**, 020408 (2010).
 - ³ C. de la Cruz, Q. Huang, J. W. Lynn, J. Li, W. R. II, J. L. Zarestky, H. A. Mook, G. F. Chen, J. L. Luo, N. L. Wang, and P. Dai, *Nature* **453**, 899 (2008).
 - ⁴ N. Ni, M. E. Tillman, J.-Q. Yan, A. Kracher, S. T. Hannahs, S. L. Bud'ko, and P. C. Canfield, *Phys. Rev. B* **78**, 214515 (2008).
 - ⁵ J.-H. Chu, J. G. Analytis, C. Kucharczyk, and I. R. Fisher, *Phys. Rev. B* **79**, 014506 (2009).
 - ⁶ N. Ni, A. Thaler, J. Q. Yan, A. Kracher, E. Colombier, S. L. Bud'ko, P. C. Canfield, and S. T. Hannahs, *Phys. Rev. B* **82**, 024519 (2010).
 - ⁷ R. M. Fernandes, L. H. VanBebber, S. Bhattacharya, P. Chandra, V. Keppens, D. Mandrus, M. A. McGuire, B. C. Sales, A. S. Sefat, and J. Schmalian, *Phys. Rev. Lett.* **105**, 157003 (2010).
 - ⁸ S. Nandi, M. G. Kim, A. Kreyssig, R. M. Fernandes, D. K. Pratt, A. Thaler, N. Ni, S. L. Bud'ko, P. C. Canfield, J. Schmalian, R. J. McQueeney, and A. I. Goldman, *Phys. Rev. Lett.* **104**, 057006 (2010).
 - ⁹ R. M. Fernandes, A. V. Chubukov, and J. Schmalian, *Nature Physics* **10**, 97 (2014).
 - ¹⁰ A. Kreyssig, M. G. Kim, S. Nandi, D. K. Pratt, W. Tian, J. L. Zarestky, N. Ni, A. Thaler, S. L. Bud'ko, P. C. Canfield, R. J. McQueeney, and A. I. Goldman, *Phys. Rev. B* **81**, 134512 (2010).
 - ¹¹ E. Hassinger, G. Gredat, F. Valade, S. R. de Cotret, A. Juneau-Fecteau, J.-P. Reid, H. Kim, M. A. Tanatar, R. Prozorov, B. Shen, H.-H. Wen, N. Doiron-Leyraud, and L. Taillefer, *Phys. Rev. B* **86**, 140502 (2012).
 - ¹² A. E. Böhmer, F. Hardy, L. Wang, T. Wolf, P. Schweiss, and C. Meingast, *Nature Communications* **6**, 8911 (2015).
 - ¹³ J. M. Allred, S. Avcı, D. Y. Chung, H. Claus, D. D. Khalyavin, P. Manuel, K. M. Taddei, M. G. Kanatzidis, S. Rosenkranz, R. Osborn, and O. Chmaissem, *Phys. Rev. B* **92**, 094515 (2015).
 - ¹⁴ E. Hassinger, G. Gredat, F. Valade, S. R. de Cotret, O. Cyr-Choinière, A. Juneau-Fecteau, J.-P. Reid, H. Kim, M. A. Tanatar, R. Prozorov, B. Shen, H.-H. Wen, N. Doiron-Leyraud, and L. Taillefer, *Phys. Rev. B* **93**, 144401 (2016).
 - ¹⁵ S. Avcı, O. Chmaissem, J. Allred, S. Rosenkranz, I. Eremin, A. Chubukov, D. Bugaris, D. Chung, M. Kanatzidis, J.-P. Castellan, J. Schlueter, H. Claus, D. Khalyavin, P. Manuel, A. Daoud-Aladine, and R. Osborn, *Nature Communications* **5**, 3845 (2014).
 - ¹⁶ L. Wang, F. Hardy, T. Wolf, P. Adelman, R. Fromknecht, P. Schweiss, and C. Meingast, *physica status solidi (b)* **254**, 1600153 (2017).
 - ¹⁷ J. M. Allred, K. M. Taddei, D. E. Bugaris, M. J. Krogstad, S. H. Lapidus, D. Y. Chung, H. Claus, M. Kanatzidis, D. E. Brown, J. Kang, R. M. Fernandes, I. Eremin, S. Rosenkranz, O. Chmaissem, and R. Osborn, *Nature Physics* **12** (2016).
 - ¹⁸ K. M. Taddei, J. M. Allred, D. E. Bugaris, S. Lapidus, M. J. Krogstad, R. Stadel, H. Claus, D. Y. Chung, M. G. Kanatzidis, S. Rosenkranz, R. Osborn, and O. Chmaissem, *Phys. Rev. B* **93**, 134510 (2016).
 - ¹⁹ K. M. Taddei, J. M. Allred, D. E. Bugaris, S. H. Lapidus, M. J. Krogstad, H. Claus, D. Y. Chung, M. G. Kanatzidis, R. Osborn, S. Rosenkranz, and O. Chmaissem, *Phys. Rev. B* **95**, 064508 (2017).
 - ²⁰ T. M. McQueen, A. J. Williams, P. W. Stephens, J. Tao, Y. Zhu, V. Ksenofontov, F. Casper, C. Felser, and R. J. Cava, *Phys. Rev. Lett.* **103**, 057002 (2009).
 - ²¹ M. D. Watson, T. K. Kim, A. A. Haghighirad, N. R. Davies, A. McCollam, A. Narayanan, S. F. Blake, Y. L. Chen, S. Ghannadzadeh, A. J. Schofield, M. Hoesch, C. Meingast, T. Wolf, and A. I. Coldea, *Phys. Rev. B* **91**, 155106 (2015).
 - ²² Q. Wang, Y. Shen, B. Pan, Y. Hao, M. Ma, F. Zhou, P. Steffens, K. Schmalzl, T. R. Forrest, M. Abdel-Hafiez, X. Chen, D. A. Chareev, A. N. Vasiliev, P. Bourges, Y. Sidis, H. Cao, and J. Zhao, *Nature Materials* **15**, 159 (2016).
 - ²³ L. Fanfarillo, J. Mansart, P. Toulemonde, H. Cercellier, P. Le Fèvre, F. Bertran, B. Valenzuela, L. Benfatto, and V. Brouet, *Phys. Rev. B* **94**, 155138 (2016).
 - ²⁴ Y. Yamakawa, S. Onari, and H. Kontani, *Phys. Rev. X* **6**, 021032 (2016).
 - ²⁵ M. A. Tanatar, A. E. Böhmer, E. I. Timmons, M. Schütt, G. Drachuck, V. Taufour, K. Kothapalli, A. Kreyssig, S. L. Bud'ko, P. C. Canfield, R. M. Fernandes, and R. Prozorov, *Phys. Rev. Lett.* **117**, 127001 (2016).
 - ²⁶ M. Chinotti, A. Pal, L. Degiorgi, A. E. Böhmer, and P. C. Canfield, *Phys. Rev. B* **96**, 121112 (2017).
 - ²⁷ M. D. Watson, A. A. Haghighirad, L. C. Rhodes, M. Hoesch, and T. K. Kim, *New Journal of Physics* **19**, 103021 (2017).
 - ²⁸ M. He, L. Wang, F. Hardy, L. Xu, T. Wolf, P. Adelman, and C. Meingast, *Phys. Rev. B* **97**, 104107 (2018).
 - ²⁹ A. E. Böhmer and A. Kreisel, *Journal of Physics: Condensed Matter* **30**, 023001 (2018).
 - ³⁰ M. Bende, A. Amato, K. Conder, M. Elender, H. Keller, H.-H. Klauss, H. Luetkens, E. Pomjakushina, A. Raselli, and R. Khasanov, *Phys. Rev. Lett.* **104**, 087003 (2010).
 - ³¹ F.-C. Hsu, J.-Y. Luo, K.-W. Yeh, T.-K. Chen, T.-W. Huang, P. M. Wu, Y.-C. Lee, Y.-L. Huang, Y.-Y. Chu, D.-C. Yan, and M.-K. Wu, *Proceedings of the National Academy of Sciences* **105**, 14262 (2008).
 - ³² J. P. Sun, K. Matsuura, G. Z. Ye, Y. Mizukami, M. Shimoza, K. Matsubayashi, M. Yamashita, T. Watashige, S. Kasahara, Y. Matsuda, J. Q. Yan, B. C. Sales, Y. Uwatoko, J. G. Cheng, and T. Shibauchi, *Nature Communications* **7**, 12146 (2016).
 - ³³ K. Miyoshi, K. Morishita, E. Mutou, M. Kondo, O. Seida, K. Fujiwara, J. Takeuchi, and S. Nishigori, *Journal of the Physical Society of Japan* **83**, 013702 (2014).
 - ³⁴ T. Terashima, N. Kikugawa, S. Kasahara, T. Watashige, T. Shibauchi, Y. Matsuda, T. Wolf, A. E. Böhmer, F. Hardy, C. Meingast, H. v. Löhneysen, and S. Uji, *Journal of the Physical Society of Japan* **84**, 063701 (2015).
 - ³⁵ K. Kothapalli, A. E. Böhmer, W. T. Jayasekara, B. G. Ueland, P. Das, A. Sapkota, V. Taufour, Y. Xiao, E. E. Alp, S. L. Bud'ko, P. C. Canfield, A. Kreyssig, and A. I. Goldman, *Nature Communications* **7**, 12728 (2016).
 - ³⁶ P. S. Wang, S. S. Sun, Y. Cui, W. H. Song, T. R. Li, R. Yu, H. Lei, and W. Yu, *Phys. Rev. Lett.* **117**, 237001 (2016).
 - ³⁷ M. Bende, A. Ichsanow, Y. Pashkevich, L. Keller,

- T. Strässle, A. Gusev, E. Pomjakushina, K. Conder, R. Khasanov, and H. Keller, *Phys. Rev. B* **85**, 064517 (2012).
- ³⁸ R. Khasanov, Z. Guguchia, A. Amato, E. Morenzoni, X. Dong, F. Zhou, and Z. Zhao, *Phys. Rev. B* **95**, 180504 (2017).
- ³⁹ A. E. Böhmer, V. Taufour, W. E. Straszheim, T. Wolf, and P. C. Canfield, *Phys. Rev. B* **94**, 024526 (2016).
- ⁴⁰ See Supplemental Material at [URL].
- ⁴¹ U. S. Kaluarachchi, V. Taufour, A. E. Böhmer, M. A. Tanatar, S. L. Bud'ko, V. G. Kogan, R. Prozorov, and P. C. Canfield, *Phys. Rev. B* **93**, 064503 (2016).
- ⁴² W. Sturhahn, *Hyperfine Interact.* **125**, 149172 (2000).
- ⁴³ R. S. Kumar, Y. Zhang, S. Sinogeikin, Y. Xiao, S. Kumar, P. Chow, A. L. Cornelius, and C. Chen, *The Journal of Physical Chemistry B* **114**, 12597 (2010).
- ⁴⁴ V. Svitlyk, M. Raba, V. Dmitriev, P. Rodière, P. Toulemonde, D. Chernyshov, and M. Mezouar, *Phys. Rev. B* **96**, 014520 (2017).
- ⁴⁵ A. E. Böhmer, T. Arai, F. Hardy, T. Hattori, T. Iye, T. Wolf, H. v. Löhneysen, K. Ishida, and C. Meingast, *Phys. Rev. Lett.* **114**, 027001 (2015).
- ⁴⁶ Q. Wang, Y. Shen, B. Pan, X. Zhang, K. Ikeuchi, K. Iida, A. D. Christianson, H. C. Walker, D. T. Adroja, M. Abdel-Hafiez, X. Chen, D. A. Chareev, A. N. Vasiliev, and J. Zhao, *Nat. Comm.* **7**, 12182 (2016).
- ⁴⁷ F. Hardy, P. Burger, T. Wolf, R. A. Fisher, P. Schweiss, P. Adelman, R. Heid, R. Fromknecht, R. Eder, D. Ernst, H. v. Löhneysen, and C. Meingast, *EPL (Europhysics Letters)* **91**, 47008 (2010).
- ⁴⁸ L. Wang, F. Hardy, A. E. Böhmer, T. Wolf, P. Schweiss, and C. Meingast, *Phys. Rev. B* **93**, 014514 (2016).
- ⁴⁹ R. M. Fernandes, D. K. Pratt, W. Tian, J. Zarestky, A. Kreyssig, S. Nandi, M. G. Kim, A. Thaler, N. Ni, P. C. Canfield, R. J. McQueeney, J. Schmalian, and A. I. Goldman, *Phys. Rev. B* **81**, 140501 (2010).
- ⁵⁰ S. Avci, O. Chmaissem, D. Y. Chung, S. Rosenkranz, E. A. Goremychkin, J. P. Castellan, I. S. Todorov, J. A. Schlueter, H. Claus, A. Daoud-Aladine, D. D. Khalyavin, M. G. Kanatzidis, and R. Osborn, *Phys. Rev. B* **85**, 184507 (2012).
- ⁵¹ S. Avci, J. M. Allred, O. Chmaissem, D. Y. Chung, S. Rosenkranz, J. A. Schlueter, H. Claus, A. Daoud-Aladine, D. D. Khalyavin, P. Manuel, A. Llobet, M. R. Suchomel, M. G. Kanatzidis, and R. Osborn, *Phys. Rev. B* **88**, 094510 (2013).
- ⁵² V. Barzykin and L. P. Gor'kov, *Phys. Rev. B* **79**, 134510 (2009).
- ⁵³ Y. Qi and C. Xu, *Phys. Rev. B* **80**, 094402 (2009).
- ⁵⁴ R. Prozorov, M. A. Tanatar, N. Ni, A. Kreyssig, S. Nandi, S. L. Bud'ko, A. I. Goldman, and P. C. Canfield, *Phys. Rev. B* **80**, 174517 (2009).
- ⁵⁵ K. Matsuura, Y. Mizukami, Y. Arai, Y. Sugimura, N. Maejima, A. Machida, T. Watanuki, T. Fukuda, T. Yajima, Z. Hiroi, K. Y. Yip, Y. C. Chan, Q. Niu, S. Hosoi, K. Ishida, K. Mukasa, S. Kasahara, J.-G. Cheng, S. K. Goh, Y. Matsuda, Y. Uwatoko, and T. Shibauchi, *Nature Communications* **8**, 1143 (2017).
- ⁵⁶ L. Xiang, U. S. Kaluarachchi, A. E. Böhmer, V. Taufour, M. A. Tanatar, R. Prozorov, S. L. Bud'ko, and P. C. Canfield, *Phys. Rev. B* **96**, 024511 (2017).
- ⁵⁷ T. Kuwayama, K. Matsuura, Y. Mizukami, S. Kasahara, Y. Matsuda, T. Shibauchi, Y. Uwatoko, and N. Fujiwara, *arXiv e-prints*, arXiv:1807.07118 (2018).
- ⁵⁸ A. V. Chubukov, M. Khodas, and R. M. Fernandes, *Phys. Rev. X* **6**, 041045 (2016).
- ⁵⁹ R. Yu and Q. Si, *Phys. Rev. Lett.* **115**, 116401 (2015).
- ⁶⁰ J. K. Glasbrenner, I. I. Mazin, H. O. Jeschke, P. J. Hirschfeld, R. M. Fernandes, and R. Valentí, *Nature Physics* **11**, 953 (2015).
- ⁶¹ D. D. Scherer, A. C. Jacko, C. Friedrich, E. Şaşıoğlu, S. Blügel, R. Valentí, and B. M. Andersen, *Phys. Rev. B* **95**, 094504 (2017).
- ⁶² J. Ishizuka, T. Yamada, Y. Yanagi, and Y. Ōno, *Journal of the Physical Society of Japan* **87**, 014705 (2018).
- ⁶³ W. R. Meier, Q.-P. Ding, A. Kreyssig, S. L. Budko, A. Sapkota, K. Kothapalli, V. Borisov, R. Valentí, C. D. Batista, P. P. Orth, R. M. Fernandes, A. I. Goldman, Y. Furukawa, A. E. Böhmer, and P. C. Canfield, *npj Quantum Materials* **3**, 5 (2018).
- ⁶⁴ W. Bi, J. Zhao, J. Lin, Q. Jia, M. Y. Hu, C. Jin, R. Ferry, W. Yang, V. Struzhkin, and E. E. Alp, *Journal of Synchrotron Radiation* **22**, 760 (2015).
- ⁶⁵ C. Meingast, F. Hardy, R. Heid, P. Adelman, A. Böhmer, P. Burger, D. Ernst, R. Fromknecht, P. Schweiss, and T. Wolf, *Phys. Rev. Lett.* **108**, 177004 (2012).
- ⁶⁶ S. Medvedev, T. M. McQueen, I. A. Troyan, T. Palasyuk, M. I. Erements, R. J. Cava, S. Naghavi, F. Casper, V. Ksenofontov, G. Wortmann, and C. Felser, *Nature Mat.* **8**, 630 (2009).
- ⁶⁷ S. Margadonna, Y. Takabayashi, Y. Ohishi, Y. Mizuguchi, Y. Takano, T. Kagayama, T. Nakagawa, M. Takata, and K. Prassides, *Phys. Rev. B* **80**, 064506 (2009).
- ⁶⁸ B. W. Lebert, V. Balédent, P. Toulemonde, J. M. Ablett, and J.-P. Rueff, *Phys. Rev. B* **97**, 180503 (2018).